Warm Pool Physics in a Coupled General Circulation Model

N. Schneider and T. P. Barnett
Climate Research Division
Scripps Institution of Oceanography
University of California at San Diego
La Jolla, California

M. Latif and T. Stockdale
Max-Planck Institute for Meteorology
Hamburg, Germany

Introduction

The warmest waters found in the open ocean are situated in the equatorial Indo-Pacific Ocean and are generally referred to as the warm pool (WP). Much could be said about the important climate processes that occur in the warm pool (e.g., World Climate Research Programme 1990), but perhaps it suffices to demonstrate the critical nature of this area by noting that the international scientific community recently concluded a large field program to elucidate the physics of the west Pacific warm pool.

As part of the modeling effort of the Atmospheric Radiation Measurement (ARM) Program, we examine in a simulation with a coupled ocean-atmosphere general circulation model (CGCM) the seasonal migration of the warm pool, its heat budget, and its relationship with radiation and clouds. The model, developed at the Max Planck Institute of Meteorology, Hamburg, couples state-of-the-art atmospheric and ocean GCM to reproduce today's climate *without* flux correction.

Coupled Model

Model Description

The coupled model, ECHO (Latif et al. 1994, Latif and Barnett 1994), used in this study consists of a sophisticated atmospheric general circulation model, ECHAM3 (Roeckner et al. 1992; DKRZ 1992) and a full nonlinear, primitive equation ocean general circulation model, the HOPE model, which is a further development of the ocean model used by Latif et al. 1993a,b. ECHAM3 has 19 levels in the vertical and was run in this study at T42 (2.8°x2.8°) resolution. The model treats the cloud water as a prognostic variable and computes air/sea heat exchange using boundary layer theory. It has been used in a variety of climate studies and has proved reliable in its ability to reproduce observed features of the tropical circulation. At T42 resolution, the wind fields mimic well the magnitude of those in observed sets (e.g., Goldenberg and O'Brien 1981).

A major failing of the model is that it underestimates the amount of low-level stratus in the eastern sides of the subtropical oceans (Latif et al. 1993a; Haskins et al., in press), which results in unrealistically warm sea surface temperatures in these regions. Perhaps a more fundamental problem is the tendency to produce double intertropical convergence zones (ITCZ), symmetric about the equator (Latif et al. 1994). We shall see below that this difficulty will be manifested also in the ocean component of ECHO, which demonstrates the coupled nature of the problem.

The ocean model (HOPE) is a further improvement of OGCMs reported in earlier studies (Latif 1987; Barnett et al. 1991; Luksch and von Storch 1992; Latif et al. 1993a, 1993b). It is a primitive equation model simplified by the hydrostatic and Boussinesq approximation. The model is global, being actively forced between 60°N and 60°S and relaxed to climatology (cf. Levitus 1982) at higher latitudes using a Newtonian formulation. The model has a rudimentary mixed layer and a Richardson-number-dependent vertical mixing scheme. The horizontal resolution is variable with latitudinal spacing of 0.5° within 10° of the equator, expanding to 2.8° resolution poleward

of 20° latitude. The longitudinal resolution is 2.8°. There are 20 levels in the vertical, 10 of which are in the upper 300 m (see Wolff and Maier-Reimer [1992] for additional details). The upper eight layers of the model are between 20 m and 25 m thick.

Several special features of the ECHO that are pertinent to this study are as follows:

- The models are coupled synchronously and do not require a flux correction term (Sausen et al. 1998) to produce a realistic climate.
- The ocean model is forced by fluxes of heat, momentum and fresh water as computed by ECHAM3. Equatorward of 60° latitude the only prescribed forcing for ECHO is the seasonally varying solar insulation at the top of the atmosphere.
- The solar radiation incident on the ocean penetrates to depth according to observations obtained by Paulson and Simpson (1977) which, on average, are highly similar to those observed during the Tropical Ocean Global Atmosphere-Coupled Ocean Atmosphere Response Experiment (TOGA-COARE) (Carter and Siegel, personal communication). About 15% of the total solar radiation penetrates beneath the 20 m surface layer of the model.

Model Performance

In this section we investigate a 2-year segment of the simulated surface radiation, clouds, and the seasonal cycle of sea surface temperature (SST), with emphasis on the seasonal cycle of the warm pool. Latif et al. (1994) and Schneider et al.[(a)] provide additional information on the performance of the ECHO.

We show in Figure 1 the annual average of the shortwave radiation at the surface of the ocean from the bulk formulae of Oberhuber (1988) and from ECHO with T42 resolution. The shortwave radiation is larger in the model than in the bulk estimates; it shows the signature of a split ITCZ and a cold tongue extending too far to the west. The longwave radiation and latent heat losses (not shown) are also larger than Oberhuber's climatology. Thus the net heat flux (Figure 2) is closer to the estimates of the bulk formulae, especially in the western Pacific, the Indian Ocean, and off

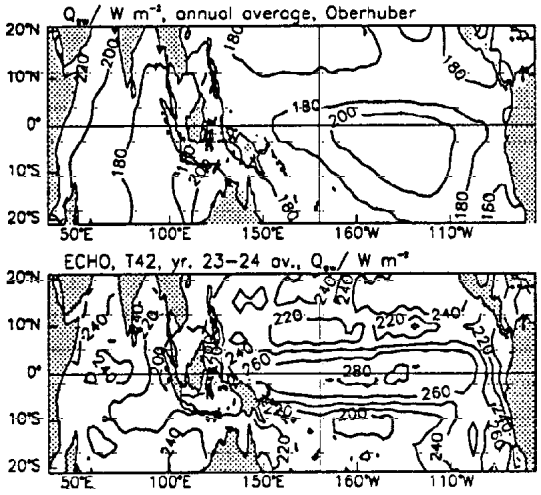

Figure 1. Annual average shortwave radiation at the sea surface for Oberhuber's (1988) climatology (top panel) and for the integration of ECHO (bottom panel).

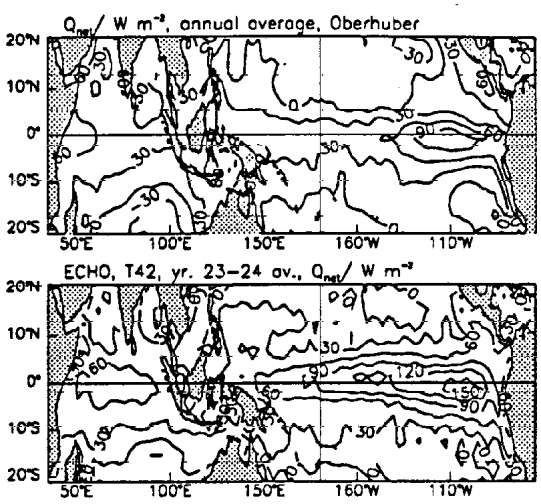

Figure 2. Annual average net heat flux at the sea surface for Oberhuber's (1988) climatology (top panel), and for the integration of ECHO (bottom panel).

the equator. However, in the cold tongue, the model ocean gains more heat compared with the bulk formulae.

The seasonal cycle of the fractional cloud cover (Figure 3) in the warm pool (10°S to 10°N, 90°E to 150°E) compares

(a) Schneider, N., T. Barnett, M. Latif, and T. E. Stockdale. Warm Pool Physics in a CGCM. Submitted to the *J. of Climate*.

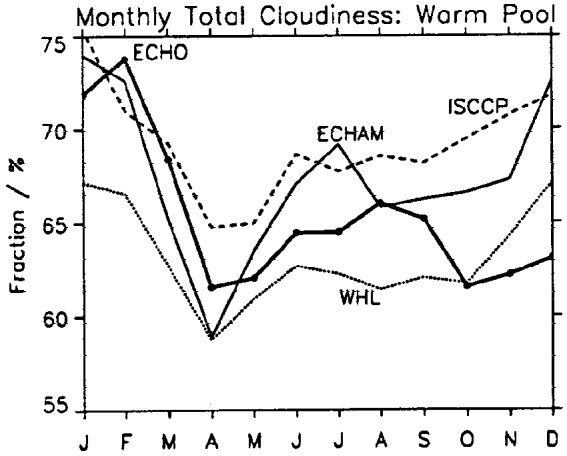

Figure 3. Seasonal cycle of cloud fraction for the coupled model (ECHO), for an atmospheric GCM (ECHAM), for satellite observations (ISCCP) and ship-based observations (WHL). ECHAM, ISCCP, and WHL data were compiled by Haskins et al. (in press).

well with estimates compiled by Haskins et al. (in press) of ship-based observations (from Warren et al. 1986, 1988), of satellite estimates (ISCCP-C2, Rossow and Schiffer, 1991) and of an atmospheric general circulation model forced by observed SSTs (Roeckner et al., 1992). Please note that ECHO and the other three estimates agree, showing a minimum in cloudiness in April.

Several aspects of the SST distribution are important for this study. Perhaps the most important is the ability of the model to reproduce the surface features of the warm pool and its seasonal motion. Figure 4 shows the SST at the extreme phases of the warm pool's seasonal migration. The upper panels show the warm pool as obtained from the observations (Reynolds 1988). The region with SST higher than 28°C is stippled, and the contour of the 28°C isotherm for each of 10 years of the observations is shown by the light lines to provide a measure of the interannual variability of the warm pool perimeter. The lower panels show the warm pool from a 2-year average of ECHO with ECHAM3 at T42 resolution.

There are obvious deficiencies: The equatorial cold tongue in the Pacific extends further to the west in the model than in the observations, and warm surface waters extend too far east in the southern hemisphere (Latif et al. 1994). The interannual variability in the observations is not large enough to explain the model-data difference. Additional analyses showed that the 2-year averages taken for the

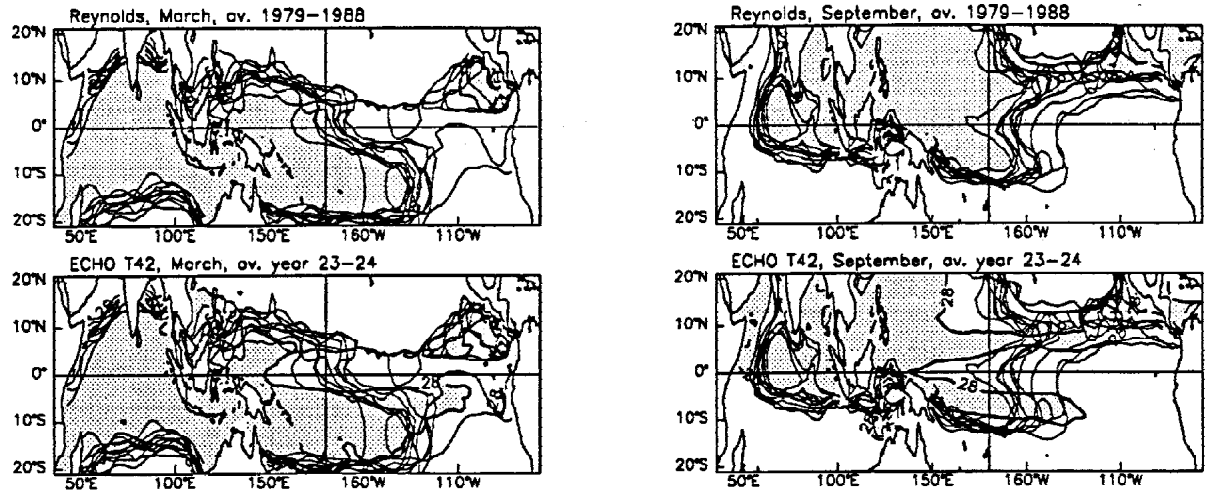

Figure 4. Waters warmer than 28°C (stippled) for the Reynolds (1988) climatology, and ECHO, for March and September. Thin lines denote the position of the 28°C isotherm for the ten years from 1979 to 1988.

model results did not represent unusually cold conditions in the extended coupled integration, so the differences are likely real. However, an enhanced cold tongue is a common feature of most OGCMs and CGCMs.

Despite these shortcomings, the seasonal migration of the warm pool is reasonably well reproduced: the main area of the warm pool is located in the fall hemisphere, both in the model and in the observations. In September, the model correctly shows the pinching off of the tongue of waters warmer than 28°C connecting the western Pacific and Central America.

Warm Pool Physics

In this section we investigate the mean and seasonal heat budget of the warm pool. We review the temperature equation, define the regions of the warm pool in the Western Pacific and the eastern Indian Ocean and present the annual average and seasonal heat budgets for a 2-year segment of a simulation with ECHO. Finding that the surface heat flux is the dominant agent for the seasonal migration of the warm pool, we determine the contributions to the net heat flux and focus on the relative roles of the short wave radiation, latent heat fluxes, and the role of clouds.

The Heat Budget

The oceanic temperature is governed by

$$\partial_t T + u\partial_x T + v\partial_y T + w\partial_z T = \left(\rho_o c_p\right)^{-1} \partial_z Q + \partial_z \overline{w' T'} + \underline{\nabla} \bullet A_h \underline{\nabla}_h T \quad (1)$$

The terms on the left-hand side of Equation (1) describe the local time (t) rate of change of temperature T and the divergence of the advective heat flux, where *x*, *y*, and *z* denote the zonal, meridional and vertical coordinates, and *u*, *v* and *w* are the respective components of the oceanic velocity. The right-hand side represents the vertical divergences of the radiative heat flux *Q*, of the turbulent heat flux $\overline{w'T'}$ and of the horizontal divergence of the fluxes due to unresolved horizontal motions (the horizontal eddy coefficient is A_h). ρ_o is a reference oceanic density, and c_p denotes the specific heat of sea water.

We consider five regions (Table 1), three of which are in the western Pacific and occupy the northern, equatorial and southern portions of the warm pool (regions N, E, S). The remaining two are located in the Indonesian waters of the Timor and Banda seas and in the eastern Indian Ocean (regions IN and I, respectively). Regions N and S were chosen to describe the seasonal cycle of the warm pool in the respective hemisphere. In region E, we determine the fluxes responsible for the westward extension of the cold tongue. Region IN looks at the importance of the Indonesian through-flow, and region I highlights difference between the western Pacific and eastern Indian ocean portions of the warm pool.

We consider the vertical integral of Equation (1) over the top 62.5 m (top 3 levels). Over this depth interval, most (98%) of the penetrative surface shortwave radiation is absorbed; i.e., for a shortwave heat flux of 230 W m^{-2}, about 4 W m^{-2} escape to deeper levels.

Table 1. Meridional and zonal boundaries of regions of the warm pool.

Region		
N	120°E - 180°	2.5°N - 8.5°N
E	120°E - 140°E	2°S - 2.5°N
S	140°E - 155°W	8.5°S - 2°S
IN	100°E - 150°E	10°S - 5°S
I	75°E - 110°E	5°S - 5°N

Mean State Physics

The annual averages of the terms in Equation (1) in the regions of the warm pool are presented in Table 2. In region N, the absorption of the surface heat flux of approximately 30 W m^{-2} is balanced mainly by upwelling induced cooling (25 W m^{-2}) and by vertical mixing (4 W m^{-2}) (Table 2). On the equator (region E), the surface heat flux of 38 W m^{-2} is counteracted by zonal advection, upwelling, and vertical mixing. The zonal advection of heat is associated with the South Equatorial Current (SEC), which brings cooler waters from the east.

Table 2. Integral over top three levels (62.5m) of the terms of the temperature equations in W m^{-2}: Annual average for years 23 and 24 of ECHO. The numbers in parentheses are the individual contributions to the total advective heat flux.

	$(\rho_o c_p)^{-1}\,\partial_z Q$	$-\underline{u}\cdot\underline{\nabla}T$			$\partial_z \overline{wT'}$	$\underline{\nabla}\cdot A_h\underline{\nabla}_h T$	$\partial_t T$
		$(-u\partial_x T$	$-v\partial_y T$	$-w\partial_z T)$			
N	29.8		-24.9		-3.8	0.0	1.1
		(3.4	-3.4	-24.8)			
E	38.1		-24.7		-12.7	-0.1	0.6
		(-9.3	-2.0	-13.4)			
S	44.4		-38.6		-5.8	-0.1	-0.2
		(-12.0	-12.1	-14.5)			
IN	31.3		-29.5		-2.9	-0.1	-1.1
		(-3.8	5.0	-32.7)			
I	51.8		-48.1		-4.6	0.0	-0.8
		(-2.0	0.7	-46.8)			

In the southern branch of the Pacific warm pool (region S), all three advective terms are of equal importance (-12 to -15 W m^{-2}) and nearly balance the surface heat flux (44 W m^{-2}). The horizontal advection of heat results from the westward flow of the SEC, the southward Ekman drift and coastal currents off New Guinea.

Region IN indicates again the main balance between the surface heat flux (31 W m^{-2}) and the vertical advection (-29 W m^{-2}). Horizontal advection heats the region only slightly: the divergence of heat transport of the Indo-Pacific through-flow is therefore small and not central for the local heat budget, even though the through-flow might be important for the global heat budget.

Finally, the eastern Indian Ocean (region I) receives the largest net surface heat flux (54 W m^{-2}), which is balanced by vertical advection.

For all regions the heat flux associated with the heat storage is much smaller than the dominant terms in the heat budget, indicating that the interannual change is small. Also, the terms due to horizontal mixing are small and are omitted in the following.

The Seasonal Cycle

As shown before, the warm pool migrates seasonally such that it is largest in the summer hemisphere. In this section, we investigate the extent to which surface flux or advection of heat controls this movement.

In the northern portion of the Pacific warm pool (region N), the surface heat flux vanishes in December and has its maximum of 58 W m^{-2} in April (Figure 5). Vertical mixing has only a small annual variability with largest cooling in December (-5 W m^{-2}) and smallest cooling in spring (-2 W m^{-2}). Advective cooling is largest in winter (-30 W m^{-2}) and has its minimum (19 W m^{-2}) in August/September. The ocean's seasonal temperature resolution (1.2°K range) is therefore largely determined by surface fluxes. Advection enhances the seasonal variability of temperature only slightly.

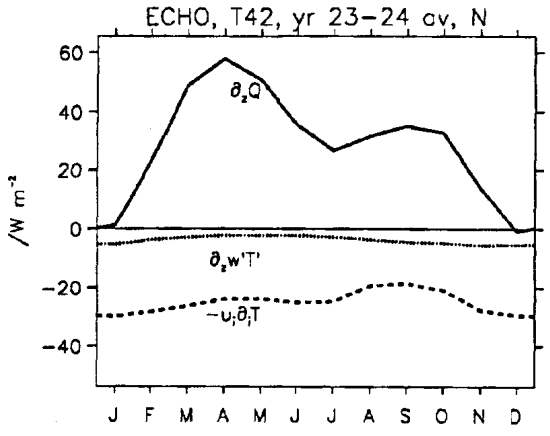

Figure 5. Contributions to the seasonal heat budget of ECHO for region N: Divergence of surface heat flux, vertical mixing, and total advection. All terms are integrated vertically over the top 62.5 m and converted to W m^{-2}.

In region E, the variability of SST is small (0.1°K range) and, for the first 9 months of the year, is governed by the semiannual signal of the advective components (not shown). In the remaining three months, the surface heat flux determines the small temperature variability.

In box S, the surface heat flux is largest in November (74 W m^{-2}) and has its minimum in July (14 W m^{-2}). The seasonal variability of the turbulent heat flux is much smaller, with a range of 7 W m^{-2}. The advective cooling is relatively constant from August to February (45 W m^{-2}), and reduces to 20 W m^{-2} heat loss in May. Again, the seasonal variability of SST (1.2°K range) is, to a large part, determined by the surface heat flux. Even though the model's south equatorial countercurrent is very strong, advection reduces the seasonal range of SST only slightly (0.2°K) and causes a phase shift of approximately one month.

In Indonesian waters (region IN), the surface and advective heat fluxes are approximately in phase, with smallest values in June and largest values at the end of the year, and with seasonal ranges of 103 W m^{-2} and 40 W m^{-2}, respectively. The turbulent component is very small. The advective components enhance the seasonal range of temperature (2.2°K) by approximately half a degree Kelvin.

The equatorially centered box in the Indian ocean (region I) displays semiannual signals of the surface heat flux, largest in April and October (66 to 81 W m^{-2}), smallest in January and August (40 and 23 W m^{-2}); very small turbulent fluxes; and an advective cooling which is constant (-50 W m^{-2}) from October to May and increases in July (-70 W m^{-2}). Thus the advective cooling reduces the seasonal range of the temperature (1.1°K), but only by 0.3°K.

In summary, we find that the surface heat flux determines the seasonal variability of upper ocean temperature in the warm pool, the only exception being the equatorial western Pacific (region E), where the seasonal range is very small. Advection increases the seasonal range of temperatures in the northern branch of the western Pacific warm pool, in the Indonesian water and in the eastern Indian Ocean. In the southern branch of the Pacific warm pool, advection counteracts the surface flux and reduces the seasonal amplitude of surface temperatures. In all cases, the advective contribution to the seasonal variability of temperature is of the order of or smaller than 0.3°K.

Surface Heat Fluxes

Because the seasonal variation of the surface heat flux is in large part responsible for the seasonal migration of the warm pool, we now investigate the annual average and seasonal cycle of the components of net heat flux. Specifically, we ask if the shortwave radiation or the latent heat flux is dominant for the seasonal cycle of the net heat flux.

The averages of the fluxes in the areas of the warm pool for the coupled model and for Oberhuber's (1988) climatology are shown in Table 3. The model shows the largest shortwave heat gains in the southern region (241 W m^{-2}) and the smallest gains in region I (181 W m^{-2}). Shortwave fluxes from the bulk formulae are smaller, but also show extreme values in region S and in the Indian Ocean. Longwave and sensible heat losses vary little between regions, where the model's variability is again larger than the climatology. The latent heat flux is smallest in the Indian Ocean in the model (-82 W m^{-2}), and large in box E (-116 W m^{-2}). The climatological latent heat loss, on the other hand, is at its minimum in the equatorial box (-75 W m^{-2}).

Even though the magnitudes of individual components are larger in the model than in the climatology, the net heat flux shows no systematic bias. This is because the overestimation of the shortwave heat gains approximately cancel the overestimation of heat losses due to evaporation and longwave fluxes.

We now turn to the seasonal cycle and present monthly changes of the components of the heat flux with their annual averages removed. In this way, the relations between individual components are most clearly seen.

In region N (Figure 6), the shortwave radiation has a strong semiannual component with largest values in April and October and smallest values in July and January. The latent heat flux is dominated by the annual period, with most negative heat fluxes in January and most reduced heat losses in June. The longwave and sensible heat fluxes are smaller. The latent and shortwave heat fluxes enhance each other from November to May, causing the net heat flux to be smallest in December and largest in April. In July, seasonally of shortwave and latent heat fluxes cancel, resulting in a zero net heat flux anomaly,

Table 3. Annual averaged surface heat fluxes in W m $^{-2}$ for years 23 and 24 of the coupled integration at T42 resolution, and, in parenthesis, for Oberhuber's (1988) climatology. Positive values indicate oceanic heating. The last two columns show the evaporative fresh water flux and precipitation in mm day^{-1}. Evaporation derived from Oberhuber's latent heat flux and precipitation estimates from the Global Precipitation Climate Project (Janowiak 1992) are given in parentheses.

Region	Q_{sw}	Q_{lw}	Q_{lat}	Q_{sens}	Q_{net}	E	P
N	225 (177)	-58 (-45)	-128 (-100)	-5 (-5)	34 (27)	4.4 (3.4)	6.1 (8.7)
E	220 (180)	-60 (-47)	-116 (-75)	-6 (-4)	38 (55)	3.9 (2.5)	3.5 (6.6)
S	241 (187)	-65 (-48)	-121 (-104)	-8 (-5)	46 (29)	4.1 (3.5)	3.6 (7.8)
IN	186 (184)	-49 (-47)	-103 (-93)	-5 (-4)	29 (40)	3.5 (3.1)	6.8 (6.0)
I	181 (174)	-49 (-45)	-82 (-89)	-4 (-4)	46 (36)	2.8 (3.0)	4.7 (11.0)

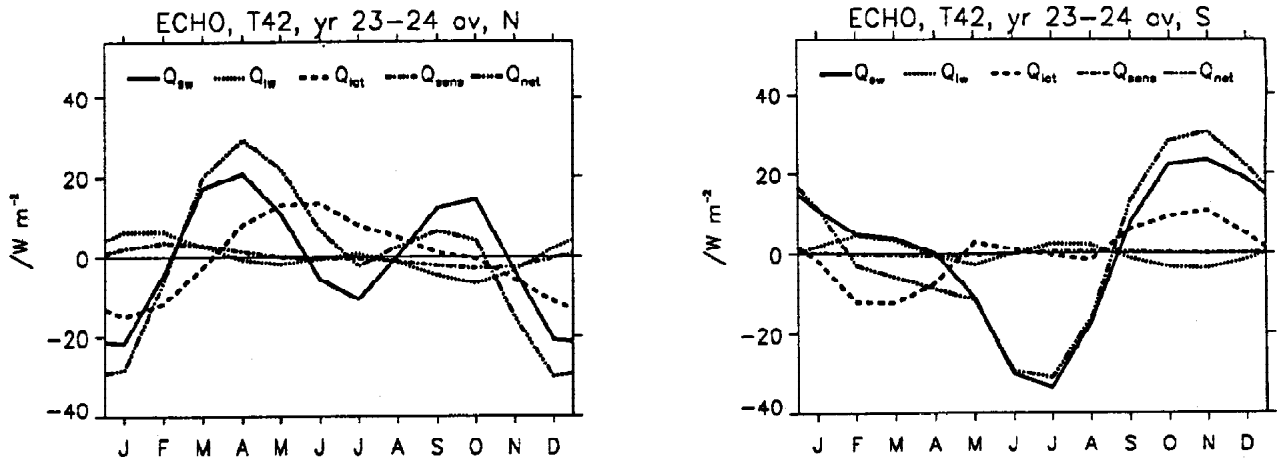

Figure 6. Seasonal cycle of the contributions to the surface net heat flux (net) due to shortwave radiation (sw), longwave radiation (lw), latent heat flux (lat), sensible heat flux (sens). Left panel shows region N, right panel region S. Units are in W m^{-2}. The annual averages of all terms have been removed.

while in October, the short wave anomaly is mitigated by the combined action of the longwave and sensible fluxes.

In region E (not shown) shortwave radiation has a semiannual signal with largest amplitudes in February (-20 W m^{-2}) and November (20 W m^{-2}). The combination of the seasonal anomalies of the latent and longwave fluxes mitigate this signal, such that the seasonal anomaly of the net heat flux is less than 10 W m^{-2}.

The seasonal anomaly of the net heat flux in region S (Figure 6) is dominated by shortwave radiation from March to December, with largest values of -35 W m^{-2}. From September to December, the shortwave signal (20 W m^{-2}) is enhanced by the residual (approximately 5 to 10 W m^{-2}) of the latent and longwave fluxes, while from January to April, the evaporative cooling counteracts the short wave and long wave components.

In region IN, the large signal of the short wave component (96 W m^{-2} range) is counteracted by the latent (40 W m^{-2} range) and long heat flux (15 W m^{-2} range) from February to May and is enhanced by the latent heat flux during the remaining time.

Finally, in region I, the semiannual signals of the short wave (73 W m^{-2} range) and latent heat fluxes (27 W m^{-2}

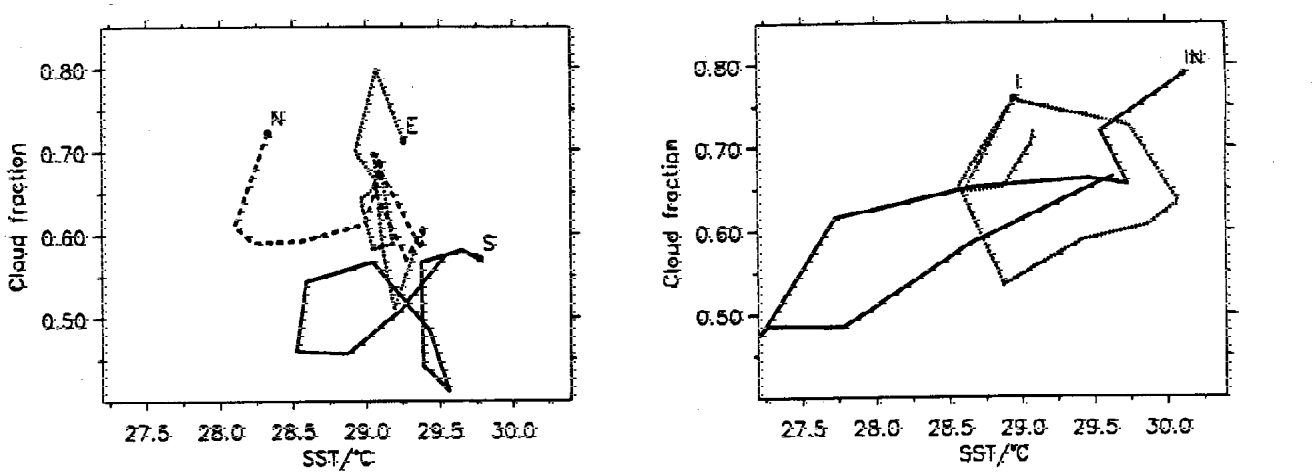

Figure 7. Seasonal evolution of SST and cloud fraction for ECHO. Curves start with January (marked by •) and end with the December. Regions are denoted by character next to the January value.

range) are in phase for most of the year, such that both contribute to the net heat flux (86 W m^{-2} range). Only in the later part of the year are the latent and shortwave anomalies of opposite signs. Furthermore, the seasonal signal is modified by the longwave component (20 W m^{-2} range).

In summary, we find that in general the shortwave radiation determines the seasonal cycle of the net heat flux, but the evaporative component modifies the signal significantly.

The Role of Clouds

The seasonal cycle of shortwave radiation is central for the seasonal migration of the warm pool. However, as seen in Figure 6, the shortwave radiation is modified by clouds, as it deviates from simple trigonometric functions expected by the astronomical forcing alone. To illustrate the relationship between SST and clouds, we show in Figure 7 the evolution of SST and cloud fraction for the five regions under consideration.

In the Pacific side of the warm pool, the seasonal evolution of the model SST and fractional cloudiness are not related in a simple manner: In regions N and S, the curves are distorted figure eights, and on the equator, changes in cloudiness are independent of temperature. Possibly nonlocal processes associated with the large gradients across the equator govern the relationship between SST and clouds.

In the Indonesian (IN) region, however, there is positive correlation between SST and fractional cloudiness, while the Indian Ocean (I) shows a double circular hysteresis curve, with SST leading by approximately 3 months. These phase relationships might indicate a local feedback between SST and clouds on a seasonal time scale.

Penetrative Radiation

The vertical structures of terms in Equation (1) reveal an important difference between the Indian Ocean area and the others. We present these terms as heating rates (units of °K $month^{-1}$), since we do not want to confuse the vertical structures by the variable vertical resolution of the model. While these units are not commonly used, they represent the vertical continuum of the effects of the fluxes.

In all areas, vertical mixing provides the link between the surface heat fluxes and vertical advection at the base of the mixed layer (Figure 8). However, the vertical structure of the divergence of the surface heat flux shows a subsurface maximum in the Pacific and Indonesian areas, but monotonically decreases with depth in the Indian Ocean (Figure 8). These vertical profiles are determined by the relative sizes of the penetrative shortwave component and heat losses at the surface (i.e., longwave and turbulent components) and represent a source of energy available to vertical mixing in the western Pacific and Indonesian waters, but not in the Indian Ocean. This is in part

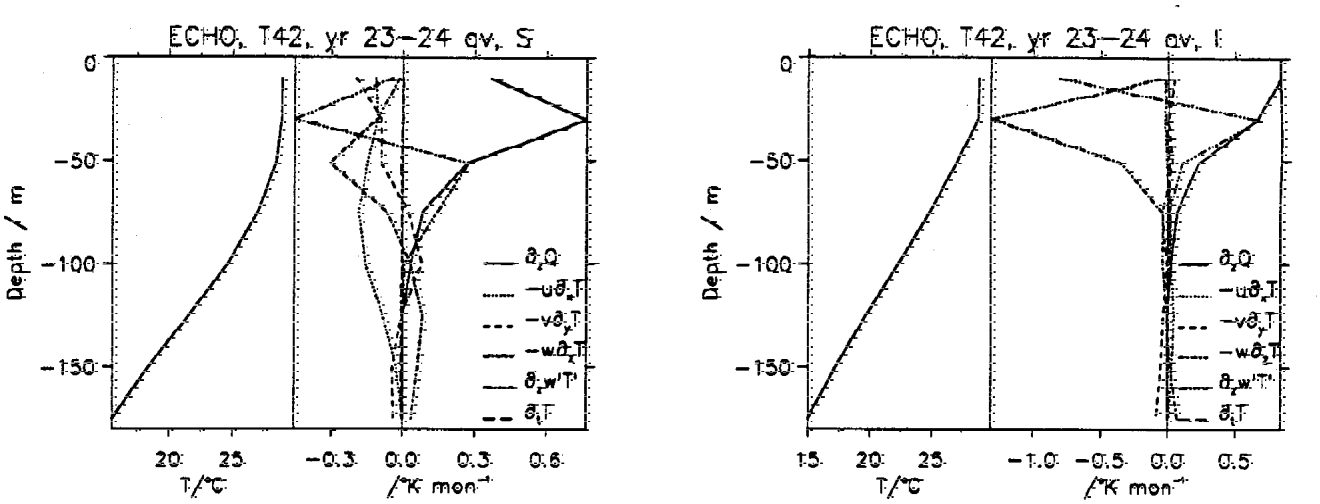

Figure 8. Annual averages of temperature (left panels) and of terms of the temperature equation (right panels), as a function of depth. Results are presented for region S (left panels), and region I (right panels).

responsible for the smaller model's upper ocean thickness in the Indian Ocean portions of the warm pool (Figure 8), as compared with the Pacific.

The observed fresh water flux (Table 3) is larger than the simulated flux and cancels this effect in region E, but not in the off-equatorial regions (Schneider et al.[(a)]).

Conclusions

In an integration of a coupled ocean atmosphere general circulation model, we have investigated the seasonal evolution of the warm pool, its heat budget, and its relationship with radiation and clouds. The model was developed at the Max-Planck Institute for Meteorology, Hamburg, and does not require a flux correction.

We found the following:

- The model has some deficiencies, most notably, the development of a double ITCZ and an equatorial cold tongue that is too strong. However, the model reproduces the seasonal migration of the warm pool reasonably well.
- The seasonal movement of the warm pool is in large part a response to the annual changes in the surface heat flux; the advective components modify the response only slightly.
- The seasonal changes of the surface heat flux are dominated by shortwave radiation, while the latent heat flux is of secondary importance.
- For the seasonal cycle, there is no clear relationship between clouds and SST in the Pacific portions of the simulated warm pool. In Indonesian waters, SST and cloudiness vary in phase, and in the eastern Indian Ocean, SSTs lead clouds by approximately 3 months.
- Destabilization of the water column due to the combination of penetrative radiation and surface cooling is a source of mixing in the deep warm pool in the western Pacific, but is absent in the shallow warm pool of the eastern Indian Ocean.

(a) Schneider, N., T. Barnett, M. Latif, and T. E. Stockdale. Warm Pool Physics in a CGCM. Submitted to the *J. of Climate*.

References

Barnett, T. P., E. Kirk, M. Latif, and E. Roeckner. 1991. On ENSO physics. *J. Climate* **4**:487-515.

DKRZ. 1992. *The ECHAM3 atmospheric general circulation model*. Deutsches Klimarechenzentrum, Hamburg, Germany, Rep. No. 6.

Goldenberg, S. B., and J. J. O'Brien. 1981. Time and space variability of the tropical Pacific wind stress. *Mon. Wea. Rev.* **109**:119-1207.

Haskins, R., T. P. Barnett, M. M. Tyree, and E. Roeckner. Comparison of cloud fields from AGCM in situ and satellite measurements. *J. Geophys. Res.,* in press.

Janowiak, J. J. 1992. Tropical rainfall: A comparison of satellite-derived rainfall estimates with model precipitation forecasts, climatologies, and observations. *Mon. Wea. Rev.* **120**:448-462.

Latif, M. 1987. Tropical ocean circulation experiments. *J. Phys. Oceanogr.* **17**: 246-263.

Latif, M., A. Sterl, E. Maier-Reimer, and H. J. Junge. 1993a. Climate variability in a coupled GCM. Part I: The tropical Pacific. *J. Climate* **6**:5-21.

Latif, M., A. Sterl, E. Maier-Reimer, and M. J. Junge. 1993b. Structure and predictability of the El Niño-Southern Oscillation phenomenon in a coupled ocean-atmosphere general circulation model. *J. Clim.* **6**:700-708.

Latif, M., T. Stockdale, J. Wolff, G. Burgers, E. Maier-Reimer, M. M. Junge, K. Arpe, and L. Bengtsson. 1994. Climatology and variability in the ECHO coupled GCM. *Tellus*., Series A, **46**:367-380.

Latif, M., and T. P. Barnett. 1994. Causes of decadal climate variability over the North Pacific and North America. *Science* **266**:634-637.

Levitus, S. 1982. Climatological Atlas of the World Ocean. NOAA Prof. Paper No. 13. U.S. Government Printing Office, Washington, D.C.

Luksch, U., and H. von Storch. 1992. Modeling the low-frequency sea surface temperature variability in the North Pacific. *J. Clim.* **5**:893-906.

Oberhuber, J. M. 1988. An atlas based on the "COADS" data set: The budgets of heat, buoyancy and turbulent kinetic energy at the surface of the global ocean. Report 15, Max-Planck-Institute for Meteorology, Hamburg.

Paulson, C. A., and J. J. Simpson. 1977. Irradiance measurements in the upper ocean. *J. Phys. Oceanogr.* **7**:952-956.

Reynolds, R. W. 1988. A real-time global sea surface temperature analysis. *J. Clim.* **1**:75-86.

Roeckner, E., K. Arpe, L. Bengtsson, S. Brinkop, L. Dumenil, M. Esch, E. Kirk, F. Lunkeit, M. Ponater, B. Rockel, R. Sausen, U. Schlese, S. Schubert, and M. Windelband. 1992. Simulation of the present-day climate with the ECHAM model: Impact of model physics and resolution. Rep. No. 93, Max-Planck-Institute für Meteorology.

Sausen, R., K. Barthel, and K. Hasselmann. 1988. Coupled ocean-atmosphere models with flux corrections. *Climate Dynamics* **2**(3):145-163.

Wolff, J., and E. Maier-Reimer. 1992. HOPE: The Hamburg Primitive Equation Ocean Model. Deutsches Klimarechenzentrum, Hamburg, Germany. Technical Report.

World Climate Research Programme. 1990. Scientific Plan for the TOGA Coupled Ocean-Atmosphere Response Experiment. WCRP Publication Series, No. 3 (Addendum), WMO/TD No. 64.